Stem Cell Research & Therapy

RESEARCH

Open Access

Stable production of immortalized hPC-MSC-derived extracellular vesicles: integrated cargo analysis and functional validation

Yingying Tong[1,2,3], Jie Sun[1,2,3], Xin Jiang[1,2,3], Xu Jia[1,2,3], Yu Jia[1,2,3], Hua Wang[4], Jiamin Wu[5], Zhuocheng Li[6], Hui Sun[7] and Guanghua Yang[1,2,3,4,5*]

Abstract

Extracellular vesicles (EVs) play a critical role in intercellular communication and have shown great potential in disease treatment and tissue repair. However, large-scale production and clinical application of EVs still face challenges such as donor heterogeneity, batch-to-batch variability, and high production costs. This study aimed to establish a stable and reproducible EV production platform using hTERT-immortalized placental mesenchymal stromal cells (PC-MSCs). We demonstrated that stable expression of the TERT gene promotes cell proliferation in vitro while retaining surface marker expression patterns and differentiation capabilities similar to those of primary cells. The EVs produced by immortalized cells maintain similar particle size distributions, protein markers, and protein expression profiles to those of their parental cells, and their therapeutic efficacy was validated in a bleomycin (BLM)-induced pulmonary fibrosis (PF) rat model. In summary, we systematically described the effect of immortalization via ectopic hTERT gene expression on EVs produced from PC-MSCs. These findings provide a new theoretical basis for the sustainable production and scale-up of EVs, as well as a new solution for the treatment of PF.

Keywords Chorionic mesenchymal stromal cells, Immortalization, Extracellular vesicles (EVs), Functional proteins, Pulmonary fibrosis (PF)

Introduction

Extracellular vesicles (EVs) are nanosized vesicles secreted by eukaryotic cells that are involved in paracrine signaling [1]. They include exosomes, microvesicles, and apoptotic bodies and carry a diverse array of bioactive molecules, including proteins, lipids, microRNAs (miRNAs), and messenger RNAs (mRNAs) [2]. EVs inherit the therapeutic properties of their parental cells and play a crucial role in intercellular communication [3]. By transferring their cargo, they regulate physiological processes and contribute to the pathogenesis of various diseases, including cancer [4, 5]. Studies have demonstrated that mesenchymal stromal cell-derived EVs exert immunomodulatory effects by regulating inflammatory responses

*Correspondence:
Guanghua Yang
ghyang119@163.com
[1]International Research Center for Biological Sciences, Ministry of Science and Technology, Shanghai Ocean University, Shanghai 201306, China
[2]National Aquatic Animal Pathogen Collection Center, Shanghai Ocean University, No. 999 Hucheng Ring Road, Shanghai 201306, China
[3]Aquatic Animal Genetics and Breeding Center, Shanghai Ocean University, Shanghai 201306, China
[4]Shanghai Telebio Biomedical Technology Co., Ltd, Shanghai 201321, China
[5]Tonglu Huayi Cell Engineering Co., Ltd, Zhejiang 311500, China
[6]The First Affiliated Hospital of Chengdu Medical College, Sichuan 610503, China
[7]Department of Oncology, Shanghai Pulmonary Hospital, Tongji University School of Medicine, Shanghai 200433, China

and immune cells and modulating fibroblast proliferation and secretory activity [6]. Through these mechanisms, EVs play a pivotal role in mediating tissue repair and regeneration.

Compared with direct mesenchymal stromal cell (MSC) therapy, EV-mediated cell-free therapy offers several advantages, including low immunogenicity and pleiotropic therapeutic effects, while mitigating the risks of tumorigenicity and infection associated with cell-based treatments [7–9]. Additionally, the accessibility of EVs significantly reduces both the time and economic costs of production. However, despite these benefits, several challenges and limitations remain in the clinical translation and large-scale application of EVs. Currently employed isolation and purification techniques lack standardized protocols, conventional cell culture methods face scalability challenges, and safety validation processes still require further optimization [10–13]. One of the most critical challenges is achieving the sustainable production of high-quality EVs with consistent cargo compositions [14]. Currently, most EV isolation strategies rely on extracting EVs from the conditioned medium of primary MSC cultures. However, the inherent tissue heterogeneity of donor-derived cells introduces variability, exacerbating batch-to-batch inconsistencies in downstream EV manufacturing. Moreover, the limited lifespan of primary MSCs poses significant challenges for large-scale production, making it difficult to obtain homogeneous EVs through continuous passaging and harvesting. EV functionality is driven primarily by the paracrine activity of parental cells, and their bioactivity is closely linked to the growth state, proliferative capacity, and lifespan of the parental cells [15, 16]. Our studies have shown that nonmutated and nonsenescent "immortalized" cell lines generated through exogenous modifications at the cellular level can serve as high-quality single-cell sources for the stable production of EVs [17]. In the continuous cultivation of cells for the harvest of EVs, immortalized cells can reduce the potential variability caused by the limited lifespan of parental cells for in vitro proliferation as well as differences between the donor batch and the potential variability caused by differences between donor lots and sources. However, the impact of the immortalization process on the secretion pathways and contents of EVs remains unclear.

To address these challenges more effectively, we investigated the potential of EVs secreted by human telomerase reverse transcriptase (hTERT)-immortalized placental chorionic mesenchymal stromal cells (hPC-MSCs) as a candidate approach. Our goal was to prevent replicative senescence and growth cessation caused by telomere shortening in primary MSCs during DNA replication by inducing the ectopic expression of the hTERT gene to activate telomerase, thus prolonging their proliferative lifespan. The placenta, often referred to as an "immune–privileged zone" of the maternal–foetal interface, represents a valuable source of high-quality MSCs. Compared with MSCs derived from bone marrow or umbilical cord blood, hPC-MSCs exhibit faster proliferation rates, greater differentiation potential, and a simpler extraction process [18]. Since the advent of hTERT-mediated immortalization, this approach has been successfully applied to various primary cells, including human MSCs, significantly extending their in vitro expansion capacity [19–21]. Although extensive literature exists on hTERT-mediated cell immortalization, its specific effects on hPC-MSCs remain underexplored. Moreover, the potential application of EVs isolated from hTERT-immortalized hPC-MSCs has yet to be thoroughly examined. We established a continuously replicating cell manufacturing platform by using a lentiviral vector to introduce the hTERT gene. This platform enables the reproducible production of EVs, which can be systematically characterized using multiple analytical approaches to evaluate their cargo compositions and biological properties.

In this study, we efficiently isolated EVs derived from hTERT-immortalized MSCs and evaluated their therapeutic potential for alleviating pulmonary fibrosis (PF) in rats. To assess the therapeutic effectiveness of EVs, we conducted a comparative analysis against two commonly used antifibrotic agents, dexamethasone (DEX) and pirfenidone (PFD), which are standard treatments for PF [22–24]. To ensure reproducibility in EV production, we generated three independent EV batches and employed a range of analytical techniques to characterize their cargo compositions and molecular properties comprehensively. Additionally, we utilized a bleomycin (BLM)-induced rat model of PF to systematically assess the effects of different doses of EVs on healthy and fibrotic lung tissue. Our findings demonstrate that EVs derived from hTERT-immortalized hPC-MSCs exhibit comparable cargo compositions and functional properties to those obtained from primary MSCs. Therefore, compared with primary MSCs, hTERT-immortalized MSCs may serve as a more consistent and scalable platform for the large-scale production of therapeutically potent EVs, offering a viable alternative for regenerative medicine applications.

Results

Successful construction of immortalized placental chorionic mesenchymal stromal cells (iPC-MSCs) with an extended lifespan

Using the pLV-IRES-hygro backbone, we successfully constructed a lentiviral plasmid overexpressing the hTERT gene (Fig. 1A), with a total length of 12,531 bp. By utilizing a second-generation lentiviral three-plasmid system, we established an hTERT gene- iPC-MSC line.

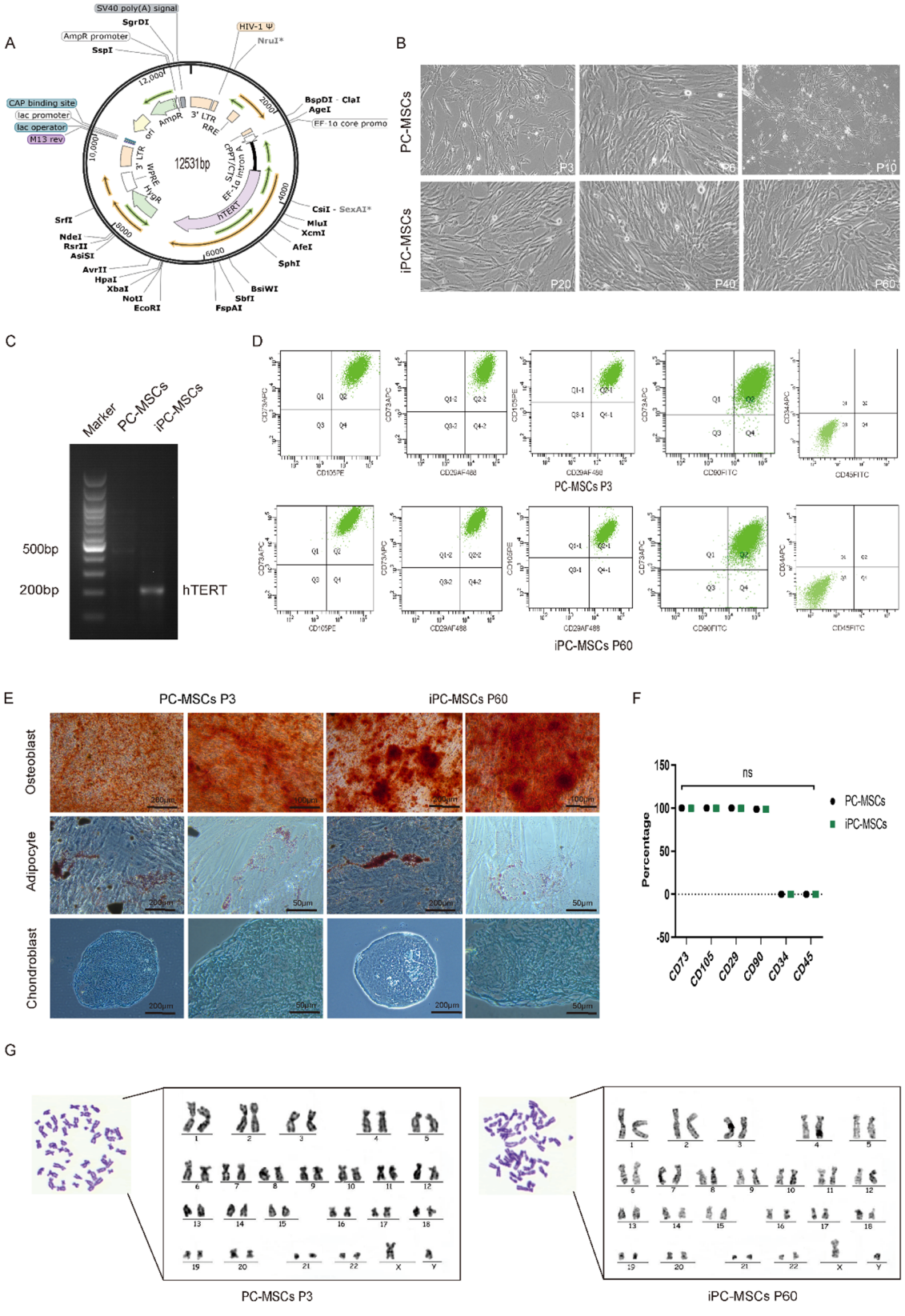

Fig. 1 (See legend on next page.)

(See figure on previous page.)

Fig. 1 Characterization of iPC-MSCs. **A** Lentiviral vector designed for overexpression of the hTERT gene. **B** Morphological comparison of PC-MSCs (p3, p6, and p10) and iPC-MSCs (p20, p40, and p60). Scale bar = 100 μm. **C** RT-PCR validation of hTERT expression in cells was performed. The hTERT amplicon length is 209 bp. PC-MSCs at passage 3 and iPC-MSCs at passage 60. The full-length gel is shown in Figure S1. **D** Analysis of PC-MSC and iPC-MSC surface antigens. Flow cytometry revealed that both cell lines were positive for the cell surface antigens CD29, CD73, CD90 and CD105 and negative for CD34 and CD45. **E** Characterization of the in vitro differentiation potential of the two cell lines. **F** Quantitative analysis of surface marker expression. The data are expressed as the means ± standard deviations (*n*=3). **G** The two cell lines presented the same karyotype before and after hTERT gene transduction

In our study, primary PC-MSCs were cultured until passage 3, the optimal growth stage, before further experimentation. In contrast, the iPC-MSCs stably proliferated for up to 60 passages without signs of senescence (Fig. 1B). Morphological analysis revealed that parental MSCs displayed the typical fibroblast-like morphology. However, after more than 10 passages, primary MSCs gradually became enlarged and flattened, which is indicative of cellular senescence [25]. In contrast, even at passage 60, the iPC-MSCs maintained a morphology highly comparable to that of the parental MSCs (Fig. 1B).

To confirm hTERT gene expression in iPC-MSCs, we extracted total RNA from both parental PC-MSCs and iPC-MSCs and performed reverse transcription PCR (RT–PCR) and agarose gel electrophoresis. The results revealed high hTERT expression in the iPC-MSC line, whereas no significant hTERT expression was detected in the parental MSCs (Fig. 1C).

These findings indicate that hTERT-overexpressing iPC-MSCs successfully bypass replicative senescence, overcoming the proliferative limitations of parental MSCs. Thus, we propose that hTERT-mediated immortalization represents a promising strategy for extending the lifespan of PC-MSCs. Further characterization and validation are warranted to assess the stability and functional properties of immortalized cells.

Unchanged cell surface marker profile in iPC-MSCs

Flow cytometry was conducted to assess the expression of cell surface markers (CD73, CD105, CD29, and CD90) and negative markers (CD34 and CD45) in iPC-MSCs at passage 60 and in 3rd-passage PC-MSCs. The results demonstrated that over 99% of both cell populations expressed the positive markers (Fig. 1D, F), whereas the expression levels of the negative markers remained below 1% (Fig. 1D, F). These findings indicate that iPC-MSCs maintain an identical surface marker profile to that of parental PC-MSCs, suggesting that the exogenous expression of hTERT does not alter the surface phenotype of immortalized cells during prolonged expansion. Furthermore, iPC-MSCs retain key stem cell characteristics, reinforcing their potential as stable and scalable MSC sources for therapeutic applications.

iPC-MSCs retain the in vitro differentiation potential of MSCs

Research has shown that MSCs retain their ability to differentiate into specific cell lineages when subjected to carefully controlled in vitro conditions [26]. To comprehensively characterize iPC-MSCs, we conducted a comparative analysis of their capacity to differentiate into osteoblasts, adipocytes, chondrocytes. Following osteogenic induction for 21 days, Alizarin Red staining revealed the formation of a mineralized extracellular matrix, confirming osteogenic differentiation (Fig. 1E). Similarly, after 21 days of adipogenic induction, intracellular lipid droplets were identified through Oil Red O staining (Fig. 1E). Furthermore, after 28 days of chondrogenic induction, Alcian blue staining highlighted the accumulation of extracellular proteoglycans, indicating successful chondrogenesis (Fig. 1E). These results demonstrate that, in addition to being an immortalized cell line, iPC-MSCs successfully retain the multipotent differentiation potential of their parental PC-MSCs, thereby meeting the minimal criteria for MSCs as defined by the International Society for Cell & Gene Therapy (ISCT) [27] .

iPC-MSCs maintain genomic stability during continuous in vitro passaging

MSCs subjected to prolonged in vitro culture or suboptimal culture conditions may exhibit genetic instability, potentially leading to karyotypic abnormalities [28]. To investigate the impact of hTERT gene integration on chromosomal stability, we conducted a comparative karyotype analysis between iPC-MSCs at passage 60 and their primary cells (Fig. 1G). Cytogenetic evaluation revealed that both cell lines maintained a normal diploid karyotype (46, XY) without detectable chromosomal aberrations. The presence of XY sex chromosomes further confirmed the male origin of the cells. These results indicate that hTERT-mediated immortalization does not lead to chromosomal instability, confirming the genetic stability of this cell line for prolonged culture use.

Both cell lines exhibit high similar gene expression profiles

To further evaluate the impact of the hTERT gene on the overall genomic pattern and potential changes in cells, we conducted RNA sequencing analysis on 3rd-passage parental PC-MSCs and 60th-passage iPC-MSCs

to explore the transcriptional alterations that may occur during immortalization.

Three parallel control groups were set up to analyse the four categories of RNA. Differential gene expression analysis was performed on the basis of the expression levels of protein-coding genes in the different samples. A total of 5165 differentially expressed genes (DEGs) were identified, including 2270 upregulated genes and 2895 downregulated genes (Fig. 2A). We visualized the overall distribution of these genes by constructing a volcano plot (Fig. 2B) and generated a heatmap of the top 20 DEGs (Fig. 2C), which were associated primarily with immune regulation processes (CSF2, IL24, CADM1, and PTGFRN) and extracellular matrix (ECM) organization

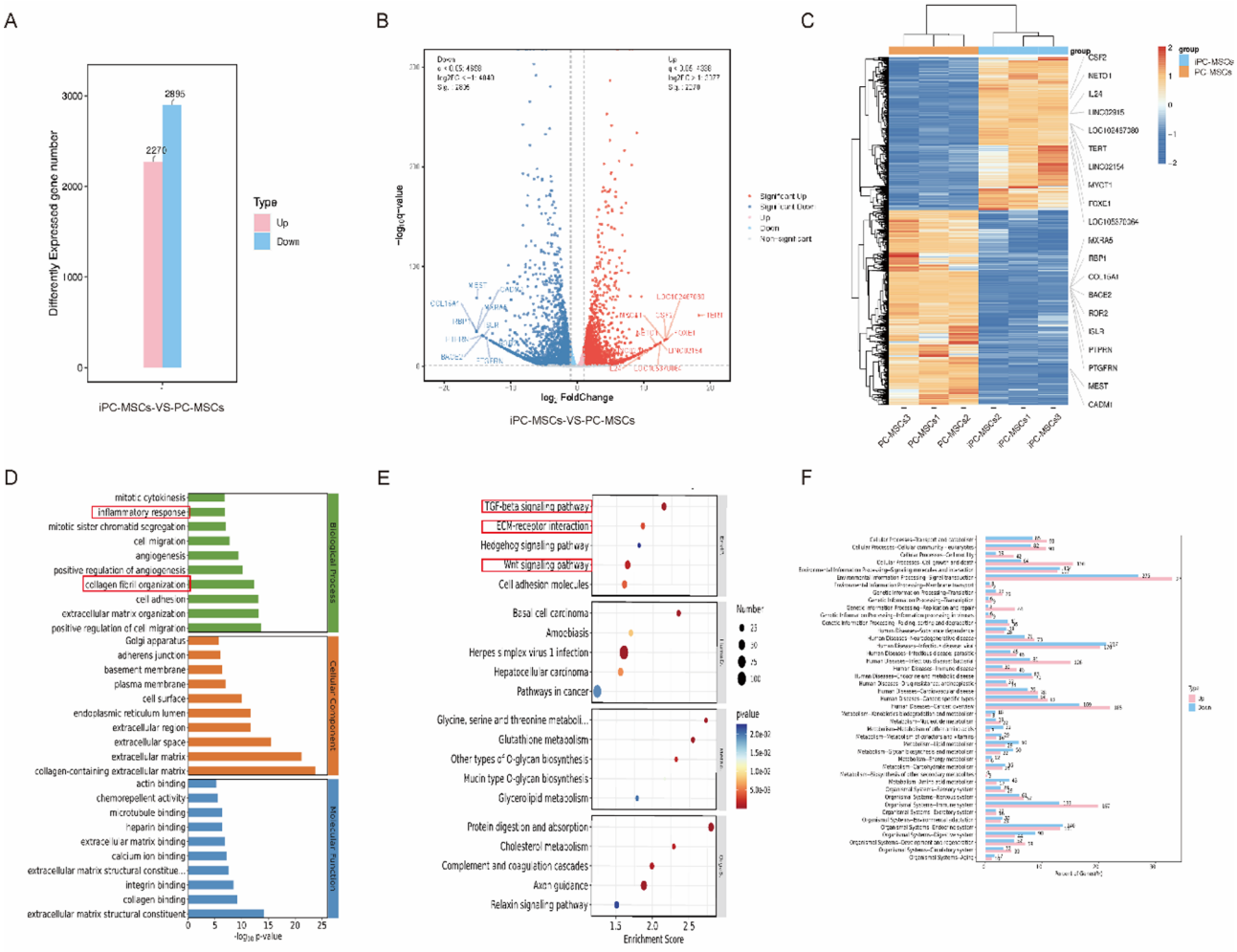

Fig. 2 Both cell lines exhibit high consistency in overall gene expression levels. **A** Quantitative distribution map of DEGs in the transcriptomes of the cell lines. **B** Volcano plot showing the gene expression differences between the cells. The grey data points correspond to nonsignificant gene fluctuations, while the red markers indicate upregulated genes, and the blue annotations denote downregulated genes. **C** Differential gene clustering heatmap. Protein-coding gene expression patterns are represented in the heatmap through a chromatic scale, where mRNA upregulation is denoted in red and downregulation appears in blue. q value < 0.05 &|log2 FC|>1. **D** GO enrichment analysis of the top 30 (total) entries is presented. Entries are sorted by −log10(p value) from largest to smallest. **E** KEGG enrichment analysis top 20 (down) bubble map. **F** Enriched KEGG pathways in the upregulated and downregulated DEGs

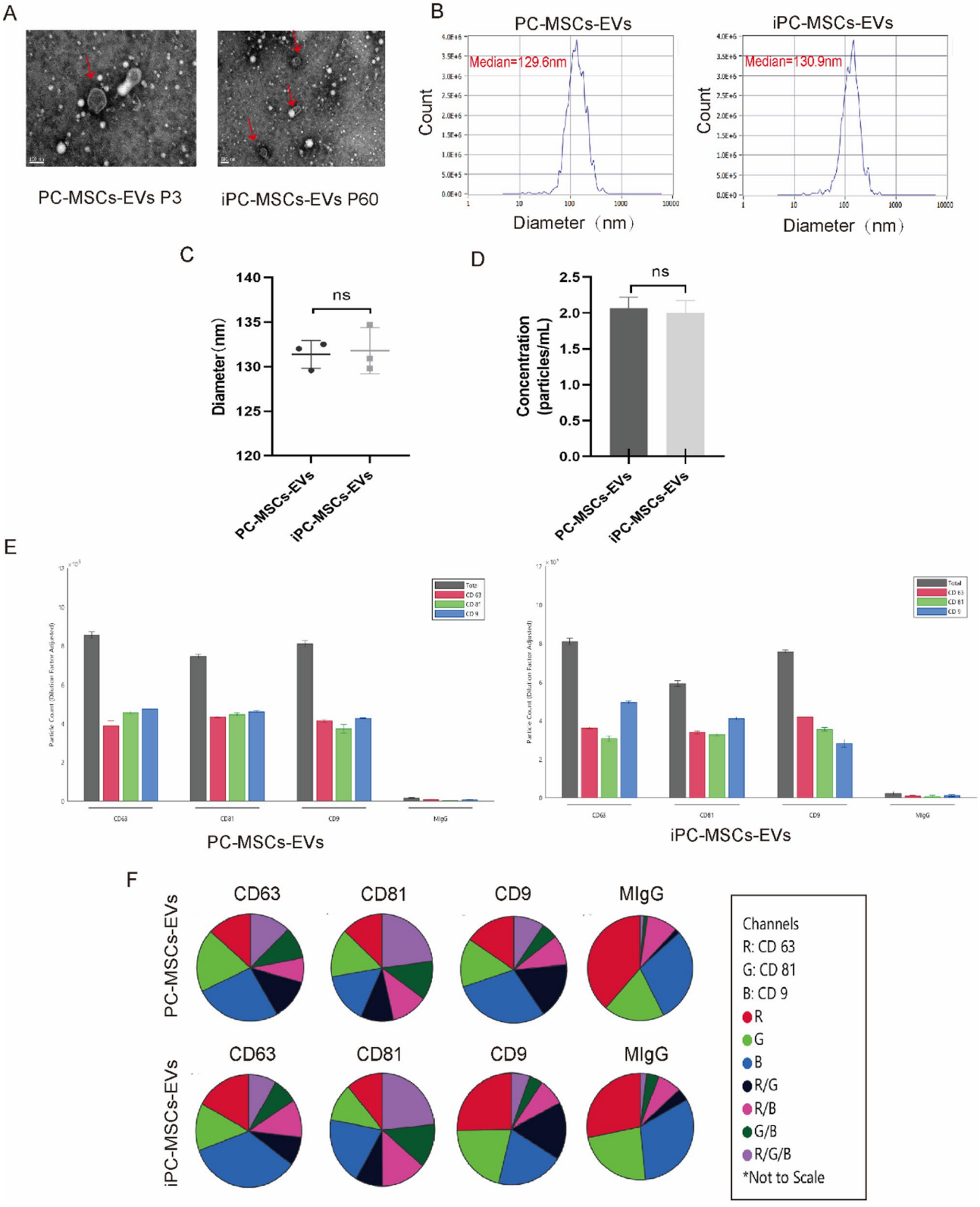

Fig. 3 (See legend on next page.)

(See figure on previous page.)

Fig. 3 Insertion of the hTERT gene does not alter the characteristics of EVs. **A** Morphology of EVs visualized by TEM. EVs from 3rd passage PC-MSCs and 60th passage iPC-MSCs were collected separately. The scale bar represents 100 nm. Red arrows denote EVs. **B** Particle size distribution of EV subpopulations. **C** Quantification of the average particle size of EVs derived from two cell lines. The data are presented as the means ± standard deviations ($n = 3$). **D** Particle concentration analysis of EVs derived from two cell lines. The data are presented as the means ± standard deviations ($n = 3$). **E** Analysis of EV subpopulation protein expression using a SP-IRIS. The data are presented as the means ± standard deviations ($n = 3$). **F** Proportion analysis of EV subpopulations. MIgG was used as a negative control

(MXRA5 and COL15A1). Notably, TERT gene expression was significantly upregulated.

Gene Ontology (GO) enrichment analysis revealed that the DEGs were associated with multiple biological processes, including inflammatory responses and collagen fibre organization (Fig. 2D). Kyoto Encyclopedia of Genes and Genomes (KEGG) pathway enrichment analysis further highlighted the signalling pathways regulated by these genes (Fig. 2E, F), including classical fibrosis-related pathways, such as the p53, TGF-β, and PI3K-AKT signalling pathways; ECM–receptor interactions; and immune-related pathways, such as the NF-κB and MAPK signalling pathways.

These findings suggest that hTERT overexpression in iPC-MSCs could modulate the immune response, inflammatory regulation, and extracellular matrix signalling pathways, potentially reducing fibrotic inflammation and improving fibrosis outcomes.

Insertion of the hTERT gene does not alter the characteristics of extracellular vesicles

Our results indicate that the insertion of the hTERT gene does not affect the efficiency of EV secretion by cells. After successful insertion of the TERT gene into the cells, the supernatant of the cell culture was collected, and EVs from the two cell lines were isolated using the PEG separation method. We examined the morphological characteristics and size distribution of EVs using transmission electron microscopy (TEM) and nanoparticle tracking analysis (NTA). Our results show that EVs derived from iPC-MSCs cultured in vitro up to the 60th passage exhibit properties similar to those of primary cells. The EVs derived from the two cell lines displayed a characteristic cup-shaped morphology (Fig. 3A), and their size distribution fell within the standard range for EVs (Fig. 3B) [29]. Analysis of three independent batches confirmed that there were no significant differences in the average particle size or concentration of EVs derived from the two cell lines (Fig. 3C and D). Moreover, the identification of protein markers using single-particle interferometric reflection imaging (SP-IRIS) technology revealed significant expression of CD63, CD81, and CD9 (Fig. 3E). The pie chart provides a more intuitive representation of the expression proportions of these proteins (Fig. 3F). Furthermore, total protein was extracted from the collected EVs and analysed using sodium dodecyl sulfate–polyacrylamide gel electrophoresis (SDS-PAGE). The results revealed that the overall protein expression profiles of the two cell lines were highly similar (Figure S2). These findings indicate that the immortalization of PC-MSCs using the hTERT gene does not notably affect the phenotype or quantity of secreted EVs.

Comprehensive proteomic profiling of EVs derived from iPC-MSCs

To obtain a complete proteomic profile of EVs derived from iPC-MSCs, we conducted a comparative proteomic analysis using EVs from PC-MSCs as the control group. Liquid chromatography–tandem mass spectrometry (LC–MS/MS) was employed for sample detection and database comparison, leading to the identification of 1,982 proteins and 16,005 peptides (Figure S3). Proteomic analysis revealed a high degree of consistency in the protein expression profiles of EVs derived from hPC-MSCs and iPC-MSCs (Fig. 4A). Although the proteomes of EVs derived from the two cell types significantly overlapped, heatmap analysis revealed specific differential features in the functional protein expression profiles of EVs derived from immortalized cells (Fig. 4B). Despite this substantial overlap, certain functionally relevant proteins were differentially expressed in EVs derived from immortalized cells (Fig. 4C). A total of 445 DEPs were identified, including 108 upregulated and 337 downregulated proteins (Figure S4). A total of 78% of the proteins coexisted in hPC-MSC-EVs and iPC-MSC-EVs. Finally, we analysed the top 20 significantly upregulated and downregulated proteins among the DEPs (Table S1).

GO functional annotation analysis revealed that the DEPs were significantly enriched in biological processes related to ribosome biogenesis (GO:0042254), translational regulation (GO:0006417), collagen fibril organization, and cell adhesion-related pathways associated with cellular immortalization (Fig. 4D). The functional characterization highlighted the differential expression of proteins involved in extracellular matrix (ECM) interactions and CXCR chemokine signalling (Fig. 4E). Notably, many upregulated proteins, including ECM proteins containing collagen domains, are associated with extracellular space function. Furthermore, KEGG pathway analysis revealed DEPs related to coronavirus disease (COVID-19) (72 proteins), IL-17 signalling (11 proteins), TNF signalling (11 proteins), and ECM–receptor interactions (14 proteins) (Fig. 4F). The differentially upregulated proteins were closely associated with the PI3K–Akt signalling pathway

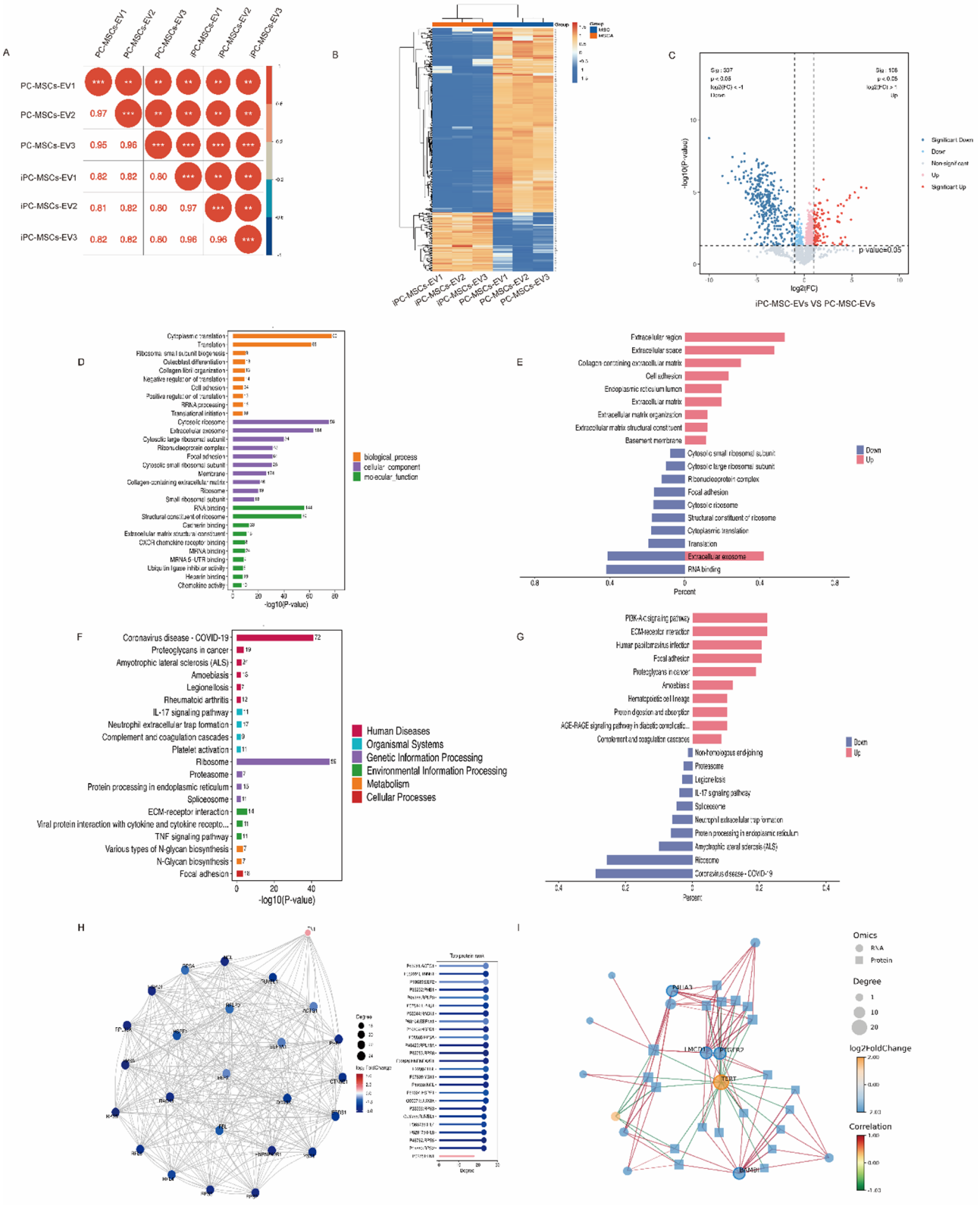

Fig. 4 (See legend on next page.)

(See figure on previous page.)

Fig. 4 Comprehensive proteomic profiling of EVs derived from iPC-MSCs. **A** Sample correlation analysis between the two cell lines. **B** Statistical analysis of protein identification in different samples. *n*=3. **C** Volcano map of DEPs. Red and blue dots indicate upregulated and downregulated proteins, respectively, with darker colours indicating more significant differences, and grey dots represent proteins with a p value ≥ 0.05. **D** GO enrichment analysis of the top 30 categories was conducted. For each of the three ontologies, ten entries were selected on the basis of a ListHits greater than 1 and the smallest p value. The number displayed on each bar represents the quantity of differential proteins annotated to that entry. **E** Comparison of up- and downregulated genes for GO enrichment analysis. The horizontal coordinate is the ratio of the number of foreground proteins to the number of background proteins for the entry (ListHits/TotalHits). **F** Distribution of DEPs at the KEGG level. **G** Comparison of up- and downregulated entries for KEGG enrichment analysis. **H** Differential protein interaction network analysis. The left panel shows a protein–protein interaction network constructed using the top 25 DEPs, the right panel shows an expression histogram of the top 25 DEPs, and the centre panel shows the shared legend of the two parts of the diagram. **I** Integrated transcriptome-proteome co-expression network. The network displays the top 20 nodes by connectivity degree from each omics layer, with only the top 5 nodes labeled. Node shapes distinguish omics types, sizes represent connectivity degrees, and the color gradient (red to blue) indicates positive to negative $\log_2$ [fold change] values

and ECM–receptor interactions, whereas the downregulated proteins were significantly associated with the COVID−19 pathway (Fig. 4G).

Further protein–protein interaction (PPI) network analysis using the STRING database predicted interactions among DEPs and revealed that fibronectin 1 (FN1) was upregulated and directly interacted with 18 downregulated proteins (Fig. 4H). As a critical ECM protein, FN1 plays a pivotal role in angiogenesis and structural organization, contributing to cell adhesion, migration, and cytoskeletal organization [30, 31]. Integrated analysis of transcriptomic and proteomic data identified the top 20 core nodes with the highest inter-sample correlation coefficients [32]. A co-expression correlation network was constructed, revealing TERT, PTGER2, LMCD1, P4HA3, and BAMBI as the top five most connected hub genes (Fig. 4I).

iPC-MSC-derived EVs exhibit no cytotoxic effects

To evaluate the therapeutic efficacy of EVs derived from iPC-MSCs on PF, we induced PF in mice through a single high-dose intratracheal administration of BLM [33]. Following PF induction, PFD, DXM, or iPC-MSC-EVs were administered intratracheally. The EVs were administered in three dose groups: 5×10^6, 5×10^7, and 5×10^8 particles per dose. After 21 days of treatment, all surviving mice were euthanized, with the exception of one animal in the low-dose and two in the mid-dose exosome groups that died from anesthetic overdose during administration. Throughout the treatment process, body weight monitoring was considered a standard measure for assessing disease burden. The rats were intrathecally injected with NaCl, PFD, DXM, or EVs, and daily body weight measurements were taken during the administration period. The results indicated that EVs had no toxic effects (Fig. 5A). As the dose of EVs increased, blood oxygen saturation, the partial pressure of oxygen (PaO_2), and the partial pressure of carbon dioxide ($PaCO_2$) increased (Fig. 5B). Notably, the therapeutic effect of EVs on $PaCO_2$ was similar to that of the positive control drugs. When the lung organ indices were compared, the BLM model control group had a greater lung index than the NC group did (Fig. 5C). Although the lung indices of the DXM group were lower than those of the BLM group were, no statistically significant differences were observed in the organ indices of the other treatment groups.

IL-1β, a proinflammatory cytokine produced primarily by macrophages and other immune cells, is crucial for regulating systemic inflammatory responses [34–36]. TGF-β, a key regulator of fibrotic processes, modulates fibroblast phenotype and function, promotes ECM accumulation, and induces myofibroblast differentiation [37]. TGF-β1, a major member of the TGF-β superfamily, is a significant driver of collagen deposition and fibrosis while also inhibiting inflammation and epithelial cell proliferation [38]. To evaluate inflammatory changes, we measured the serum levels of IL-1β and TGF-β1 in different groups of rats (Fig. 5D). Compared with those in the DXM and PFD groups, IL-1β levels were elevated in all EV-treated groups, although these differences were not statistically significant. TGF-β1 levels were elevated in the BLM group compared with the NC group, with a similar trend observed in the 5×10^8 EV group. Conversely, the TGF-β1 levels were lower in the other treatment groups than in the BLM group.

EVs from iPC-MSCs significantly attenuate pulmonary fibrosis in rats

On the basis of the proteomic analysis results, we investigated whether iPC-MSCs could ameliorate BLM-induced PF in rats by modulating collagen deposition. We established an EV-mediated therapeutic protocol in rats to evaluate the in vivo effects of different EV doses. When EVs derived from iPC-MSCs were administered during the fibrotic phase, they effectively mitigated fibrotic inflammation and alleviated BLM-induced lung injury. Notably, the therapeutic efficacy of iPC-MSC-EVs was comparable to that of the standard antifibrotic drugs DXM and PFD.

Histopathological examination of haematoxylin and eosin (HE)-stained sections from both the control and EV-treated groups revealed fibrotic damage alleviation to varying degrees (Fig. 6A). The medium- and high-dose EV groups presented denser alveolar structures

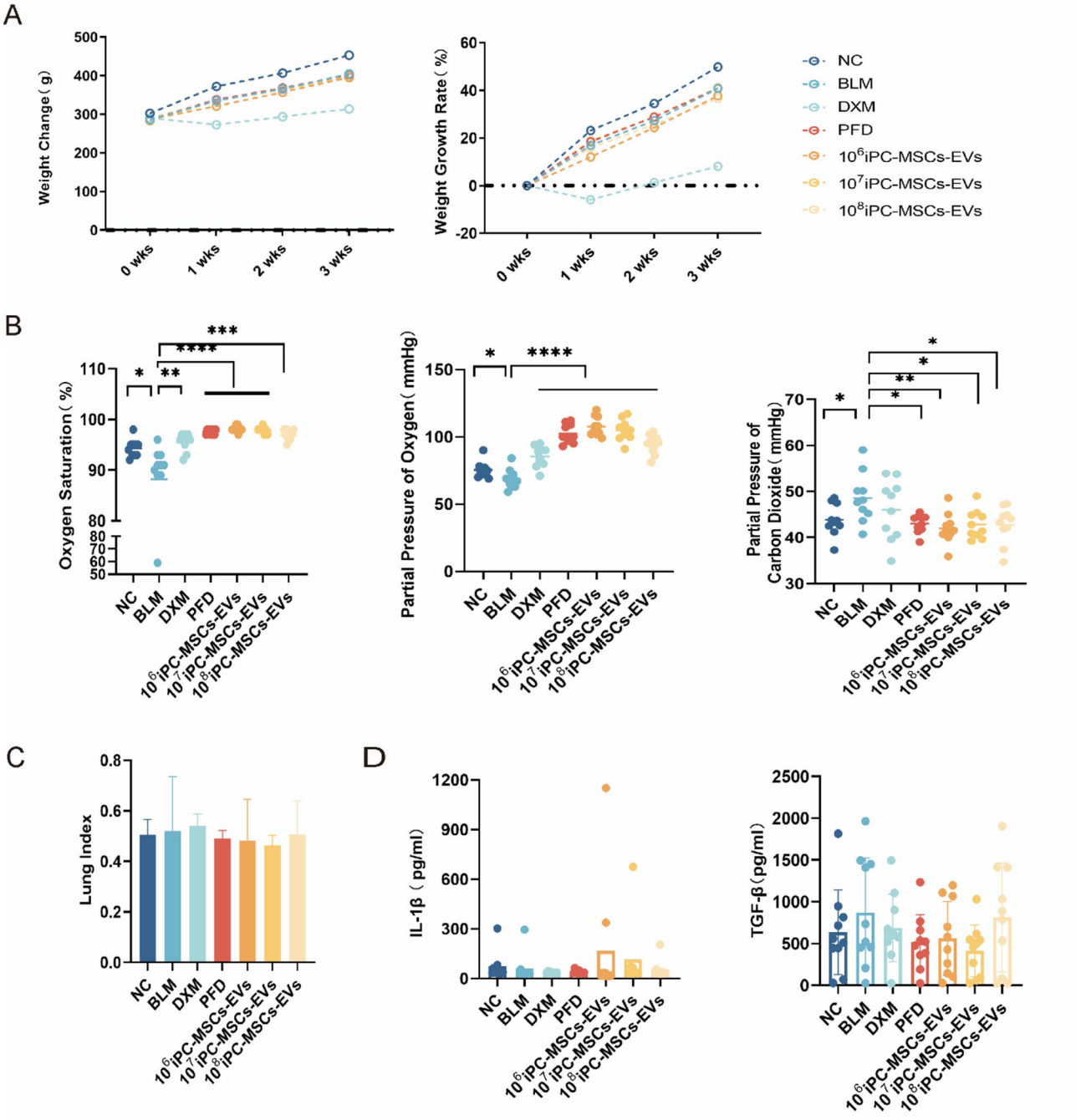

Fig. 5 iPC-MSC-derived EVs exhibit no cytotoxic effects. **A** Body weight change and body weight growth rate of rats. Each group of rats $n = 10$, and the following experimental data of each group were expressed as the means ± standard deviations and statistically tested by one-way analysis of variance (ANOVA). **B** The results of the rat blood gas analysis, in order of oxygen saturation, partial pressure of oxygen, and partial pressure of carbon dioxide. **C** Rat lung tissue organ index. **D** Serum levels of TGF-β1 and IL-1β. No statistically significant difference in components

and reduced areas of lung injury. In contrast, lung tissue sections from the BLM-treated group presented disrupted alveolar architecture, with fewer regular alveolar spaces and bullae formed by ruptured alveolar walls. The positive control drug treatment groups presented thickened alveolar walls and substantial pulmonary consolidation with irregular alveoli. Pathological scoring was significantly greater in the BLM group than in the control group, while both DXM and EV treatments decreased these scores (Fig. 6C). The fibrosis score indicated mild to moderate fibrotic changes in the lungs of BLM-treated rats, with significantly lower Ashcroft scores observed in both the DXM and EV treatment groups than in the BLM group (Fig. 6D, Tables S2, S3). Furthermore, Masson's

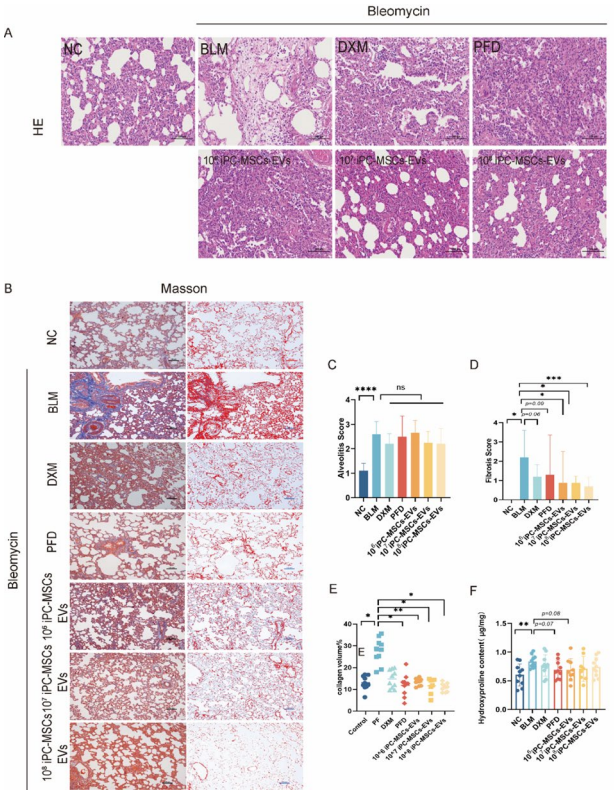

Fig. 6 EVs from iPC-MSCs Significantly Attenuate PF in Rats. **A** Typical image of lung histopathology with HE staining. **B** A typical image of Masson staining. Fibrotic lesions were stained blue. **C** Alveolitis scores for each drug treatment group. **D** Fibrosis scores for each drug treatment group. **E** Collagen volume statistics after Masson staining of lung tissue. **F** Hypoxyproline content in lung tissue. There were 10 rats in each group, and the experimental data of each group are expressed as the means ± standard deviations and were statistically tested by one-way analysis of variance (ANOVA)

trichrome staining of lung tissue sections revealed significantly increased collagen fibre content in the BLM-treated group (Fig. 6B). Notably, the administration of different EV doses to BLM-treated rats substantially reduced collagen fibre deposition (Fig. 6E). Specifically, the deposition levels in the low-, medium-, and high-dose groups were reduced by 51.6%, 57.7%, and 60.5%, respectively, compared to the BLM group. The therapeutic outcomes achieved by EV treatment were comparable to those of both the control and positive drug treatment groups.

To quantitatively evaluate the antifibrotic effects of EVs, we measured the levels of hydroxyproline, a specific marker of collagen deposition in fibrotic tissues. Compared with that in normal controls, the hydroxyproline content in BLM-induced fibrotic lungs was significantly elevated (Fig. 6F). Both the PFD-treated and low-dose EV groups presented significantly lower hydroxyproline levels. While the intergroup differences did not reach statistical significance, potentially owing to experimental duration limitations, these findings demonstrate that EV treatment attenuates BLM-induced PF, as evidenced by reduced collagen deposition and alleviated fibrotic pathology.

Discussion

In this study, we conducted high-resolution proteomic analysis of EVs derived from TERT gene-transduced immortalized MSCs. Our findings demonstrate that (a) EVs from immortalized MSCs maintain comparable morphological characteristics, including size, density, and surface molecular markers, to those from primary cells; (b) while the proteomic profiles of MSC-derived EVs show substantial similarity, immortalized cells exhibit distinct protein signatures compared with their primary counterparts; and (c) EVs derived from iPC-MSCs possess significant antifibrotic properties. This study provides the first preliminary introduction of proteomic differences between EVs from immortalized and primary MSCs, elucidates their therapeutic potential for PF treatment, and offers novel insights into scalable EV production and clinical applications.

During this research, we aimed to establish a stable cell line and obtain homogeneous EVs for PF research. To achieve this goal, we developed iPC-MSCs using the pLVX-IRES-Hyg lentiviral vector combined with TERT expression. iPC-MSCs provide a consistent and stable source of EVs derived from stem cells. We showed that stable expression of the TERT gene promotes cell proliferation in vitro. Our results demonstrate that iPC-MSCs expressing ectopic hTERT successfully bypass the Hayflick limit observed in primary PC-MSCs, extending their lifespan. Under standard culture conditions, primary cells undergo replicative senescence by the 10th passage, while iPC-MSCs can be continuously passaged up to the 60th passage without losing their normal morphology. After antigenic analysis and differentiation assays, the iPC-MSCs retained their stem cell properties, which was consistent with previous studies [39]. It is important to consider potential safety risks when using lentiviral vectors for cell transduction [40]. Long-term culture may also affect the safety of the cells and their secreted products [41]. To assess the stability and safety of iPC-MSCs, we conducted karyotype analysis. The results revealed that the chromosome structure of iPC-MSCs, even at passage 60, remained consistent with that of third- passage parental cells, confirming the genetic stability of these cells over extended culture.

RNA-seq data analysis revealed significant changes in the signalling pathways of iPC-MSCs, with immortalization notably affecting the regulation of key inflammatory pathways, including P53, NF-κB, and MAPK. NF-κB plays a central role in regulating telomerase activity, primarily through controlling the nuclear translocation

process. This process is largely driven by the induction of tumour necrosis factor (TNF) [42, 43]. In our study, the upregulation of TNF and alterations in the NF-κB pathway in immortalized iPC-MSCs provided strong evidence for the role of posttranscriptional regulation in this process. Furthermore, iPC-MSCs significantly inhibited ECM−receptor interactions and the Wnt signalling pathway. Given that abnormal ECM accumulation is a key pathological feature of PF [22, 44] and that TERT mutations leading to telomere shortening are closely associated with the development of idiopathic pulmonary fibrosis (IPF), these findings suggest that iPC-MSCs overexpressing hTERT may enhance resistance to the fibrotic process through unique molecular mechanisms, despite the full regulatory mechanisms remaining unclear. These results indicate that iPC-MSCs could serve as high-quality cell sources for cell-based therapies, potentially overcoming the challenges of cost and batch variability associated with different cell types. The ectopic expression of TERT may confer superior resistance to fibrosis in both the cells and their secreted products.

We conducted a comparative analysis of EVs derived from both iPC-MSCs and primary cell lines. The EVs from both cell lines exhibited highly similar morphologies, particle size distributions, and protein markers. These characteristics are consistent with the definition of EVs outlined in the MISEV2018 guidelines [45]. These findings indicate that EVs inherit surface features from their parental cells. However, owing to the insertion of the TERT gene, EVs may encapsulate different contents and exhibit distinct functional properties. Proteomic analysis revealed differences in the protein profiles of EVs derived from MSCs and iPC-MSCs. The differentially expressed proteins between the two cell lines were linked to immune regulation and ECM interactions, which was consistent with the results from the transcriptomic analysis.

Numerous studies have demonstrated that EVs derived from MSCs from various sources can prevent fibrosis by reducing collagen accumulation and inhibiting fibroblast proliferation [46–48]. However, few studies have explored the antifibrotic effects of EVs derived from immortalized cells. In this study, we used a bleomycin-induced PF rat model to investigate the effects of EVs derived from immortalized cells on lung inflammation. To evaluate the therapeutic efficacy of EVs, we selected two positive drugs as controls and tested three different doses of EVs in preliminary experiments. Our results show that EVs derived from iPC-MSCs significantly alleviated BLM-induced PF in rats, offering protective and therapeutic effects during the processes of lung inflammation and tissue damage. We verified these findings using several methods, including histological analyses such as HE and Masson's trichrome staining, in Wistar rats. After the tracheal administration of iPC-MSCs, collagen deposition and the extent of fibrosis were reduced, and EV treatment notably diminished these phenotypic changes in the lung tissue. After treatment with iPC-MSC-EVs, the hydroxyproline level in the lung tissue significantly decreased. All three EV dosage groups showed improvement trends similar to those of the PFD treatment group and outperformed those of the DXM group. Hydroxyproline, a key structural component of collagen, is a marker that reflects the extent of collagen synthesis during fibrosis and indirectly indicates the severity of PF [49]. Interestingly, we observed varying effects across different EV doses in a rat model of lung injury. In the range of 5×10^6 to 5×10^7 particles, the high-dose group demonstrated superior resistance to fibrosis. However, at a high dose of 5×10^8 particles, a negative correlation between dose and therapeutic efficacy was observed. This phenomenon has been confirmed in clinical evaluations of EV efficacy [50].

These results suggest that EVs derived from iPC-MSCs exhibit strong antifibrotic properties and have high potential for clinical application in the treatment of PF. Furthermore, this study validated the use of iPC-MSCs as a reliable and consistent source for the production of EVs. Importantly, appropriate dosing is crucial for maximizing the therapeutic effects of iPC-MSCs. Previous reports have shown that exosome lipids have lipophilic properties that enhance the delivery of antifibrotic drugs such as PFD [51] to the lungs. The excellent biocompatibility and tissue-targeting ability of these EVs provide a promising foundation for the development of drug delivery platforms for PF treatment [52]. Moreover, immortalization enhances the potential for high-throughput EV production and rapid clinical application.

Due to the lack of direct functional data on hPC-MSC-EVs in PF, it is challenging to precisely assess the differences in therapeutic efficacy and potential unique characteristics of iPC-MSC-EVs. Although the antifibrotic effects of iPC-MSC-EVs have been observed, and proteomic analysis has suggested potential active molecules and pathways, these omics findings have not yet been validated through functional experiments, limiting the exploration of their mechanism of action. In addition, the final process for testing the efficacy of iPC-MSC-EVs is still imperfect, and although evidence from animal models is available for support, human application inevitably varies, making it difficult to ensure maximum benefit to patients in clinical trials. In conclusion, iPC-MSCs with ectopic expression of the TERT gene can serve as high-quality alternative cell sources for large-scale production of EVs. The shape, size, density, and surface molecular characteristics of EVs derived from these cells are similar to those of the primary cells, but they also have antifibrotic effects. This study suggests that EVs from immortalized MSCs could represent promising

therapeutic agents and provides evidence for their potential clinical application in pulmonary diseases.

Methods

Animals

PF was induced in Wistar rats (6 weeks old, male, body weight 200–220 g, specific pathogen-free (SPF) grade). This study was approved by the Experimental Animal Ethics Committee of Shanghai Pharmaceutical Industry Research Institute Co., Ltd. (Approval Number A20230602) and was in line with ARRIVE guidelines 2.0. The animals were kept in the SPF-level animal house of Shanghai Research Institute of Pharmaceutical Industry Co., Ltd. (Experimental Animal Licence: SYXK (Shanghai) 2019-0027). All the animals were kept under standard animal housing conditions (temperature: 20–26 °C; relative humidity: approximately 40–70%; 12 h light/dark cycle; air exchange frequency: 15 times/h), in line with the People's Republic of China national standard GB14925-2010 environmental requirements. The animals were kept under normal routine conditions with free access to food and water.

Human placental MSC culture

hPC-MSCs at passages 0 to 2 were provided by Shanghai Telebio Biomedical Technology Co., Ltd [17]. Both the original hPC-MSCs and iPC-MSCs were cultured in MSCBM (6114021, Shanghai Dakowei, China) devoid of EVs and serum and supplemented with 4% EV-free PLT-Gold® Human Platelet Lysate (#PITGold500R, Sartorius, Germany) and 1% penicillin/streptomycin. Cultures were grown at 37 °C in a 5% CO_2 environment. Passaging was performed every 48 h, and the cells were subcultured upon reaching 80%-90% confluence. For passaging and experimental analyses, the cells were dissociated with 0.5% trypsin solution (15400-054, Gibco).

Development of an iPC-MSC line

To establish an immortalized cell line, we utilized a second-generation lentiviral three-plasmid system to infect parental cells. The plasmid encoding the overexpressed hTERT gene was synthesized by QuanYang Biotechnology Co., Ltd., and was tailored for our experimental needs. The 293T cell line, along with the lentiviral packaging plasmids psPAX2 (Addgene, ID #12260) and PMD2. G (Addgene, ID #12259), were provided by Shanghai Telebio Biomedical Technology Co., Ltd. The pLVX-IRES-Hyg vector (ID #632185) served as the backbone for plasmid construction, incorporating the EF1α promoter and XbaI-NheI cloning sites. BamHI and EcoRI restriction enzyme sites flanking the hTERT gene were added according to its sequence characteristics. The plasmid also contained a hygromycin resistance gene.

For viral packaging, 293T cells were transfected with 10 μg of transfer plasmid, 6.5 μg of envelope plasmid (PMD2. G), and 8.5 μg of packaging plasmid (psPAX2) [40, 53]. The virus titres were determined using an integration assay, and the viral titre reached 3×10^8 TU/mL, resulting in an infection efficiency of approximately 80%. Prior to viral infection, primary PC-MSCs were seeded in six-well plates and passaged twice to achieve optimal growth conditions. A total of 3×10^6 cells were infected with 500 μL of recombinant lentivirus. The cells were gently mixed and incubated at 37 °C for 12–24 h, after which fresh MSC culture medium was added. Selection for hygromycin resistance was initiated 72 h post infection, with 1 μg/mL hygromycin added to the medium. A control group of primary cells was used for comparison. The selection process continued for 15 days, with complete medium containing hygromycin being refreshed every 3–4 days. The selected cells, which survived after the control group was entirely eliminated, were considered immortalized target cells.

RNA extraction, cDNA synthesis, and PCR

Total RNA was extracted from cells using an RNA Extraction Kit (#R0024, Beyotime Biotechnology, Shanghai, China) according to the manufacturer's protocol. Briefly, 300 μL of lysis buffer was added to 5×10^5 cells to ensure complete lysis of the samples. The purity and concentration of the extracted RNA were then determined using a NanoDrop 2000 spectrophotometer (Thermo Scientific, USA). The lysate was mixed with an equal volume of binding buffer, transferred to a purification column, and centrifuged to remove impurities. The column was thoroughly washed with washing buffer, followed by high-speed centrifugation to eliminate residual liquid. Finally, the RNA was eluted by adding elution buffer, incubating at room temperature, and centrifuging to obtain purified RNA. The purity and concentration of the RNA were determined using a NanoDrop 2000 spectrophotometer (Thermo Scientific, USA) [54]. The integrity of the RNA was analysed using an Agilent 2100 Bioanalyzer (Agilent Technologies, Santa Clara, CA, USA). cDNA libraries were constructed using a BeyoRT™ II First Strand cDNA Synthesis Kit (#D7168M; Beyotime Biotechnology, Shanghai, China) following the manufacturer's instructions. PCRs were conducted with 2× Hieff PCR Master Mix premixed with the following primers: Forward (5′-3′): CTGAGTATGGCTGCGTGGTGAAC and Reverse (5′-3′): GTTGAAGGTGAGACTGGCTCTGATG.

Transcriptome sequencing and differential gene expression analysis

Transcriptome sequencing was conducted by Shanghai OE Biotech Co., Ltd. (Shanghai, China). Using the Illumina NovaSeq 6000 platform, 150 bp paired-end

reads were generated by sequencing. The raw data were filtered using the fastp tool [55], and high-quality clean reads were selected for subsequent analysis [56]. Reference genome alignment and gene expression levels, measured in fragments per kilobase of transcript per million mapped reads (FPKM), were calculated using the HISAT2 software [57]. Principal component analysis (PCA) of gene expression counts was performed using R (v3.2.0) to assess biological replicates. DEGs were identified by the DESeq2 software [58], with a q value < 0.05 and a fold change >1 used as the criteria for identifying DEGs. GO enrichment and KEGG pathway analyses were performed using the hypergeometric distribution method to identify significantly enriched functional categories. Finally, gene set enrichment analysis (GSEA) was conducted to identify whether predefined gene sets were enriched at the top or bottom of the ranked list of DEGs between the two sample groups.

Flow cytometric profiling

When the cells reached the logarithmic growth phase, they were harvested and prepared as a cell suspension at a final concentration of 1×10^6 cells/mL. Antibody incubation buffer and 5 μL of monoclonal antibody (BioLegend, USA) were added to the cell suspension. A total of five positive markers were detected, including CD90 (FITC), CD29 (AF488), CD73 (APC), and CD105 (PE), along with two epithelial markers, CD34 (APC) and CD45 (FITC). The cell–antibody mixture was incubated in the dark at room temperature for 20 min. After incubation, the cells were thoroughly washed before analysis. Flow cytometry was performed using a BD FACS Celesta (BD FACS Celesta, BD, USA), and the data were recorded and analysed with FlowJo v10.8.1 software.

Cell differentiation assays

MSCs were induced to differentiate into osteogenic, adipogenic, and chondrogenic lineages using the Human-Associated Stem Cell-Induced Differentiation Kit (Cyagen, Guangzhou, China) according to the manufacturer's instructions for preparing the induction media. Parental cells and iPC-MSCs were seeded at a density of 1×10^5 cells per well in 24-well plates and subjected to osteogenic and adipogenic differentiation protocols.

Osteogenic differentiation was initiated using an osteogenic induction kit (#HUXXC-90021, Cyagen, Guangzhou, China) when the cell confluence reached 70%. Fresh OriCell® osteogenic induction medium was replaced every 3 days, and the induction period lasted for 21–27 days. The formation of round calcified nodules was observed, and the cells were then fixed in 10% formalin for 30 min at room temperature, followed by gentle washing 2–3 times. The cells were stained with Alizarin Red solution at room temperature for 5–10 min.

Adipogenic differentiation was initiated using an adipogenic induction kit (#HUXXC-90031, Cyagen, Guangzhou, China). The induction medium was prepared according to the manufacturer's instructions, with medium A and medium B used alternately every 3 days and 1 day, respectively, over a period of 21–27 days. The formation of lipid droplets in the cytoplasm was observed. The culture medium was removed, and the cells were fixed in 10% formalin at room temperature for 30 min, followed by staining with Oil Red O.

Chondrogenic differentiation was induced using the chondrogenic induction medium (#HUXXC-90041; Cyagen, Guangzhou, China) under 3D culture conditions to form chondrospheres [59, 60]. A total of 3×10^5 cells were seeded in 15 mL centrifuge tubes to begin the chondrogenic differentiation protocol. After 24–48 h of incubation, the tubes were gently tapped to suspend the chondrospheres in the medium. The induction medium was replaced with fresh medium every 3 days. On day 28, the chondrospheres were fixed with 10% formalin for 30 min at room temperature, followed by gradient dehydration with alcohol. After xylene treatment, the chondrospheres were embedded in paraffin and sectioned at 3 μm. The sections were stained with Alcian blue at 37 °C for 1 h to assess chondrogenic differentiation.

Chromosomal karyotyping

Cells in the logarithmic growth phase were selected and treated with colchicine (final concentration of 0.2 μg/mL), followed by gentle mixing and incubation at 37 °C for 1–2 h. The cells were then digested with trypsin, followed by centrifugation at 800×*g* to collect the cell pellet. The pellet was resuspended in an appropriate volume of prewarmed isotonic solution (0.075 M KCl, prepared by dissolving 44.7 mg of KCl in 8 mL of sterile water), gently mixed, and incubated in a 37 °C water bath for 40 min. After incubation, 2 mL of fixative solution (methanol: glacial acetic acid = 3:1) was added, and the mixture was incubated at room temperature for 10 min before centrifugation at 500×*g*. The supernatant was discarded, and the cell pellet was resuspended in fresh fixative for an additional 10 min. This washing procedure was repeated three times. The fixed cell suspension (10 μL/drop) was dropped onto precleaned glass slides and dried at 75 °C for 2–3 h. After the slides were completely dry, they were subjected to brief digestion in freshly prepared 0.25% trypsin for 1 min (with strict time control). The slides were then stained with Giemsa solution for 5–10 min, followed by rinsing with running water to remove excess stain. Chromosome analysis was performed under a microscope to observe the results.

Isolation and characterization of extracellular vesicles

For the 3rd-passage PC-MSCs and 60th-passage iPC-MSCs, EVs in the supernatant of the cell culture medium were isolated by polyethylene glycol 8000 (PEG, #P2139, Sigma, Germany) precipitation when the cell growth density reached 80% [61]. Briefly, the cell supernatant was centrifuged in a gradient and added to the prepared 5×PEG 8000 solution, which was gently mixed every 20–30 min, which was repeated 3–5 times, and left to stand at 4 °C for 12–24 h. Subsequently, the mixed solution was centrifuged at 4000×*g* at 4 °C for 40 min, and the resulting precipitate was filtered aseptically through 0.45 μm filters to obtain the EV samples, which were stored at − 80 °C for storage.

An FEI Tecnai G2 F20 transmission electron microscope (Thermo Fisher, USA) was used to image the EV mixture for morphological observation. A single sample volume of 20 μL was used, and three cycles (10 positions per cycle) were set up: focal length 100 nm, sensitivity 70.0, shutter speed 70, and frame rate 20. The particle size distributions of the obtained samples were analysed using NTA. Analysis of EV subpopulation protein expression using a single-particle interferometric reflectance imaging sensor (SP-IRIS). The samples were processed according to the manufacturer's protocol. EV samples were diluted with sample buffer at a 1:1 ratio such that the final sample concentration ranged from 1×10^7 to 1×10^8/mL. Fifty microlitres of the diluted sample was added dropwise to the ExoView R200 chip and incubated at room temperature for a total of 16 h. At the end of the incubation, the chip was shaken and rinsed with 1000 μL of incubation buffer at 200 × g for 3 min, and the process was repeated three times. The chip was subsequently incubated with staining solution containing antibodies against CD9 (CF488A), CD81 (CF555), and CD63 (CF647) for 1 h in the dark, shaken slowly, and washed sequentially with incubation buffer and deionized water. After complete drying, the microarrays of the chip were imaged using an ExoView R200 scanner (NanoView, Boston, MA, USA). The raw data were analysed using NanoViewer 2.8.10 software.

Protein extraction and bioinformatics analysis of EVs

Protein extraction was performed using ultrasound-assisted cell disruption. Briefly, EVs were treated with 1 mM phenylmethylsulfonyl fluoride (PMSF) to inhibit proteolytic activity. After ultrasonic disruption, the samples were centrifuged at 12,000 rpm for 10 min at 4 °C to pellet the cellular debris. This step was repeated once, and the supernatant containing solubilized proteins was collected for further analysis. Protein quantification was performed using the BCA assay (Thermo Scientific). Electrophoresis was conducted on 12% SDS–polyacrylamide gels. After protein separation, the gels were stained with Coomassie Brilliant Blue using the eStain LG protein stainer and imaged with an automated digital gel imaging system.

High-resolution mass spectrometric analysis was performed using liquid chromatography–tandem mass spectrometry (LC–MS/MS)

The extracted proteins were quantified using the BCA method. A nanoElute liquid chromatography system (Bruker Daltonics) with a reversed-phase column was subsequently applied for gradient elution of the protein peptides. The separation took 90 min at a flow rate of 500 nL/min on a C18 analytical column (ID 1.6 μm C18, Ion Opticks).Two buffers were used, with Buffer A containing 0.1% formic acid (FA) in water and Buffer B containing 0.1% FA in ACN. The obtained data were analysed using the Spectronaut Pulsar 18.4 (Biognosys). Feature expression matrices from both omics datasets were integrated using the mixOmics toolkit, followed by correlation analysis of the derived features.

BLM-induced pulmonary injury model and therapeutic intervention

The 70 animals were divided into a NC group (10 animals) and a treatment group (60 animals). The treated Wistar rats were injected with BLM at a dose of 2.5 mg/kg by tracheal administration through the centripetal end of the tracheal cartilage ring gap. The treated rats were stratified by body weight and randomized through a sequence generated by the RAND function in Microsoft Excel into BLM treatment group, positive control group (DXM group, PFD group), and iPC-MSC-EV group (high, medium, and low doses), and each group consisted of 10 rats. The NC group was injected with saline alone, the BLM treatment group was given saline after successful modelling, and the remaining groups were given the corresponding drugs after successful modelling. The iPC-MSC-EV group was divided into 3 dose groups: the high-, medium-, and low-dose groups (5×10^8 pcs/pc, 5×10^7 pcs/pc, and 5×10^6 pcs/pc). Drug administration was started 7 days after modelling and was repeated every other day for a total of 10 doses until 21 days after modelling. On the basis of the results of the previous experiments in our laboratory, the effect of PFD alone was not obvious in the positive control drug group, so DXM was added as a positive control drug. After 7 days of modelling, 0.6 mg/kg DXM and 200 mg/kg PFD were administered once daily until 21 days after modelling.

Histopathological examination

After the rats were anaesthetized using 3% isoflurane by intraperitoneal injection at the endpoint of the experiment, blood was taken from the abdominal aorta for blood gas analysis. Rats were euthanized by cervical

dislocation. Whole lungs were removed from the rats after necropsy to determine the lungs and calculate the organ index. The lungs were repeatedly lavaged with 2 mL of sterile saline, and the lung lavage fluid was collected for the detection of inflammatory cells (haematology) and inflammatory factors (TGF-β1 and IL-1β). The lung tissues were subsequently fixed in 10% formaldehyde solution until the pleura spread, the bronchial tubes were subsequently ligated, and samples were taken longitudinally from the tip to the base of the lungs for pathologic examination. All histopathological evaluations were performed by a pathologist blinded to the experimental groups. After haematoxylin–eosin (HE) staining, inflammation in the lung tissue was evaluated using the Szapiel scoring system and Ashcroft score. The alveolar morphology of the rats in each experimental group was observed under a microscope after Masson staining.

Hydroxyproline quantification assay

The hydroxyproline content was measured using a kit acquired from Nanjing Jian Bioengineering Institute following the manufacturer's. After the animal was sacrificed, the material was removed from one side of the lung and freeze-dried for 12 h, after which the moisture was removed. Five hundred microlitres of alkaline lysis solution was added to 40 mg of lung tissue sample and hydrolysed in boiling water for 20 min. The pH of the reaction mixture was adjusted to 6.0–6.8, and activated charcoal was added to treat the reaction mixture. The mixture was then centrifuged to collect the supernatant, which was then mixed with the assay agent and incubated in a water bath at 60 °C for 15 min, after which the optical density (OD) at 550 nm was measured in each well.

Statistical analysis

The optimal sample size was determined based on a statistical analysis of results from similar PF studies. Data are presented as the means ± standard deviations. Statistical analysis was performed using GraphPad Prism 8.0.2. Statistical comparisons among multiple groups were performed using one-way analysis of variance (ANOVA), followed by post hoc tests for multiple comparisons where appropriate. In cases where the data violated the assumption of normality or equal variances, an appropriate non-parametric test (the Kruskal-Wallis test) or a data transformation was applied instead. A p-value of less than 0.05 was considered statistically significant.

Supplementary Information

The online version contains supplementary material available at https://doi.org/10.1186/s13287-025-04743-2.

Supplementary Material 1.

Acknowledgements

The authors declare that they have not use AI-generated work in this manuscript.

Author contributions

Yingying Tong: Conceptualization, methodology, software, validation, formal analysis, investigation, data curation, visualization, writing—original draft, writing—review & editing. Jie Sun: validation, investigation, formal analysis, writing—original draft, writing—review & editing. Xin Jiang: formal analysis, investigation, software, writing—review & editing. Xu Jia: validation, investigation, data curation, writing—original draft. Yu Jia: visualization, writing—review & editing. Hua Wang: investigation, data curation, formal analysis. Jiamin Wu: investigation, validation. Zhuocheng Li: writing—review & editing. Hui Sun: writing—review & editing. Guanghua Yang: methodology, formal analysis, visualization, supervision, writing–review & editing, resources project, administration, funding acquisition.

Funding

This research did not receive any specific grant from funding agencies in the public, commercial, or not-for-profit sectors.

Data availability

The transcriptomics raw sequence data reported in this paper have been deposited in the Genome Sequence Archive in National Genomics Data Center, China National Center for Bioinformation / Beijing Institute of Genomics, Chinese Academy of Sciences (GSA-Human: HRA013406) that are publicly accessible at https://ngdc.cncb.ac.cn/gsa-human.The proteome data reported in this paper have been deposited in the OMIX, China National Center for Bioinformation / Beijing Institute of Genomics, Chinese Academy of Sciences (https://ngdc.cncb.ac.cn/omix: accession no. OMIX012060).

Declarations

Ethics approval and consent to participate

Shanghai Telebio Biomedical Technology Co., Ltd., the source of the human cells used in this study, has confirmed that initial ethical approval was obtained for their collection and that informed consent was provided by all donors. The experimental animals used in this study were approved by the Animal Ethics Committee of Shanghai Institute of Pharmaceutical Industry Co., Ltd. The project titled "Compound Treatment of Bleomycin-Induced Pulmonary Fibrosis in Rats" with approval number A-2023-06-02 was granted on August 7, 2023.

Inclusion and diversity statement

We support inclusive, diverse, and equitable conduct of research.

Competing interests

The authors declare no competing interests.

Received: 21 May 2025 / Accepted: 9 October 2025
Published online: 05 November 2025

References

1. Colombo M, Raposo G, Thery C. Biogenesis, secretion, and intercellular interactions of exosomes and other extracellular vesicles. Annu Rev Cell Dev Biol. 2014;30:255–89. https://doi.org/10.1146/annurev-cellbio-101512-122326.
2. Raposo G, Stoorvogel W. Extracellular vesicles: exosomes, microvesicles, and friends. J Cell Biol. 2013;200:373–83. https://doi.org/10.1083/jcb.201211138.
3. Weng Z, et al. Therapeutic roles of mesenchymal stem cell-derived extracellular vesicles in cancer. J Hematol Oncol. 2021Sep 3;14(1):136. https://doi.org/10.1186/s13045-021-01141-y
4. Raposo G, Nijman HW, Stoorvogel W, Liejendekker R, Harding CV, Melief CJ, Geuze HJ. B lymphocytes secrete antigen-presenting vesicles. J Exp Med. 1996;183(3):1161–72. https://doi.org/10.1084/jem.183.3.1161.
5. Fujita Y, Yoshioka Y, Ochiya T. Extracellular vesicle transfer of cancer pathogenic components. Cancer Sci. 2016;107:385–90. https://doi.org/10.1111/cas.12896.

6. Shentu TP, et al. Thy-1 dependent uptake of mesenchymal stem cell-derived extracellular vesicles blocks myofibroblastic differentiation. Sci Rep. 2017;7:18052. https://doi.org/10.1038/s41598-017-18288-9.
7. Beer L, Mildner M, Ankersmit HJ. Cell secretome based drug substances in regenerative medicine: when regulatory affairs Meet basic science. Ann Transl Med. 2017;5:170. https://doi.org/10.21037/atm.2017.03.50.
8. Zeng Y, et al. Biological features of extracellular vesicles and challenges. Front Cell Dev Biol. 2022;10:816698. https://doi.org/10.3389/fcell.2022.816698.
9. Moloudizargari M, Asghari MH, Goel A. The therapeutic triad of extracellular vesicles: as drug targets, as drugs, and as drug carriers. Biochem Pharmacol. 2021;192:114714. https://doi.org/10.1016/j.bcp.2021.114714.
10. Gelibter S, et al. The impact of storage on extracellular vesicles: A systematic study. J Extracell Vesicles. 2022;11:e12162. https://doi.org/10.1002/jev2.12162.
11. Azkargorta M, et al. Human serum extracellular vesicle proteomic profile depends on the enrichment method employed. Int J Mol Sci. 2021;22(20):11144. https://doi.org/10.3390/ijms222011144
12. Gupta D, Zickler AM, El Andaloussi S. Dosing extracellular vesicles. Adv Drug Deliv Rev. 2021;178:113961. https://doi.org/10.1016/j.addr.2021.113961.
13. Saad MG, Beyenal H, Dong WJ. Exosomes as powerful engines in cancer: Isolation, characterization and detection techniques. Biosens (Basel). 2021. https://doi.org/10.3390/bios11120518.
14. Kimiz-Gebologlu I, Oncel SS, Exosomes. Large-scale production, isolation, drug loading efficiency, and biodistribution and uptake. J Control Release. 2022;347:533–43. https://doi.org/10.1016/j.jconrel.2022.05.027.
15. Lin Y, Zhu W, Chen X. The involving progress of MSCs based therapy in atherosclerosis. Stem Cell Res Ther. 2020;11:216. https://doi.org/10.1186/s13287-020-01728-1.
16. Li J, Ge Z, Ji W, Yuan N, Wang K. The proosteogenic and proangiogenic effects of small extracellular vesicles derived from bone marrow mesenchymal stem cells are attenuated in steroid-induced osteonecrosis of the femoral head. Biomed Res Int. 2020;2020:4176926. https://doi.org/10.1155/2020/4176926
17. Tong Y, et al. A study on the production of extracellular vesicles derived from novel immortalized human placental mesenchymal stromal cells. Sci Rep. 2025. https://doi.org/10.1038/s41598-025-87371-3.
18. Pethe P, Kale V, Placenta. A gold mine for translational research and regenerative medicine. Reprod Biol. 2021;21:100508. https://doi.org/10.1016/j.repbio.2021.100508.
19. Bodnar AG, et al. Extension of life-span by introduction of telomerase into normal human cells. Science. 1998;279:349–52. https://doi.org/10.1126/science.279.5349.349.
20. Nisato RE, et al. Generation and characterization of telomerase-transfected human lymphatic endothelial cells with an extended life span. Am J Pathol. 2004;165:11–24. https://doi.org/10.1016/S0002-9440(10)63271-3.
21. Piera-Velazquez S, Jimenez SA, Stokes D. Increased life span of human Osteoarthritic chondrocytes by exogenous expression of telomerase. Arthritis Rheum. 2002;46:683–93. https://doi.org/10.1002/art.10116.
22. Thannickal VJ, Toews GB, White ES, Lynch JP, Martinez FJ. Mechanisms of pulmonary fibrosis. Annu Rev Med. 2004;55:395–417. https://doi.org/10.1146/annurev.med.55.091902.103810.
23. Wuyts WA, et al. First data on efficacy and safety of nintedanib in patients with idiopathic pulmonary fibrosis and forced vital capacity of </=50 % of predicted value. Lung. 2016;194:739–43. https://doi.org/10.1007/s00408-016-9912-1.
24. King TE Jr., et al. A phase 3 trial of Pirfenidone in patients with idiopathic pulmonary fibrosis. N Engl J Med. 2014;370:2083–92. https://doi.org/10.1056/NEJMoa1402582.
25. He Q, Ye Z, Zhou Y, Tan WS. Comparative study of mesenchymal stem cells from rat bone marrow and adipose tissue. Turk J Biol. 2018;42:477–89. https://doi.org/10.3906/biy-1802-52.
26. Khan WS, Hardingham TE. Mesenchymal stem cells, sources of cells and differentiation potential. J Stem Cells. 2012;7:75–85.
27. Viswanathan S, et al. Mesenchymal stem versus stromal cells: international society for cell & gene therapy (ISCT(R)) mesenchymal stromal cell committee position statement on nomenclature. Cytotherapy. 2019;21:1019–24. https://doi.org/10.1016/j.jcyt.2019.08.002.
28. Bai Q, et al. Temporal analysis of genome alterations induced by Single-Cell passaging in human embryonic stem cells. Stem Cells Dev. 2015;24:653–62. https://doi.org/10.1089/scd.2014.0292.
29. Chernyshev VS, et al. Size and shape characterization of hydrated and desiccated exosomes. Anal Bioanal Chem. 2015;407:3285–301. https://doi.org/10.1007/s00216-015-8535-3.
30. Saatci O, et al. Targeting Lysyl oxidase (LOX) overcomes chemotherapy resistance in triple negative breast cancer. Nat Commun. 2020;11(1):2416. https://doi.org/10.1038/s41467-020-16199-4
31. Liu C, et al. Heterogeneous microenvironmental stiffness regulates pro-metastatic functions of breast cancer cells. Acta Biomater. 2021;131:326–40. https://doi.org/10.1016/j.actbio.2021.07.009.
32. Tamo L, et al. Gene network analysis of interstitial macrophages after treatment with induced pluripotent stem cells secretome (iPSC-cm) in the bleomycin injured rat lung. Stem Cell Rev Rep. 2018;14:412–24. https://doi.org/10.1007/s12015-017-9790-9.
33. Izbicki G, Segel MJ, Christensen TG, Conner MW, Breuer R. Time course of bleomycin-induced lung fibrosis. Int J Exp Pathol. 2002;83:111–9. https://doi.org/10.1046/j.1365-2613.2002.00220.x.
34. Mantovani A, Barajon I, Garlanda C. IL-1 and IL-1 regulatory pathways in cancer progression and therapy. Immunol Rev. 2018;281:57–61. https://doi.org/10.1111/imr.12614.
35. Conti P, et al. Coronavirus-19 (SARS-CoV-2) induces acute severe lung inflammation via IL-1 causing cytokine storm in COVID-19: a promising inhibitory strategy. J Biol Regul Homeost Agents. 2020;34:1971–5. https://doi.org/10.23812/20-1-E.
36. Gabryelska A, Kuna P, Antczak A, Bialasiewicz P, Panek M. IL-33 mediated inflammation in chronic respiratory Diseases-Understanding the role of the member of IL-1 superfamily. Front Immunol. 2019;10:692. https://doi.org/10.3389/fimmu.2019.00692.
37. Biernacka A, Dobaczewski M, Frangogiannis NG. TGF-beta signaling in fibrosis. Growth Factors. 2011;29:196–202. https://doi.org/10.3109/08977194.2011.595714.
38. Wei Y, et al. Fibroblast-specific Inhibition of TGF-beta1 signaling attenuates lung and tumor fibrosis. J Clin Invest. 2017;127:3675–88. https://doi.org/10.1172/JCI94624.
39. Lee KM, Choi KH, Ouellette MM. Use of exogenous hTERT to immortalize primary human cells. Cytotechnology. 2004;45:33–8. https://doi.org/10.1007/s10616-004-5123-3.
40. Sakuma T, Barry MA, Ikeda Y. Lentiviral vectors: basic to translational. Biochem J. 2012;443:603–18. https://doi.org/10.1042/bj20120146.
41. Nam H, et al. Effects of Long-Term in vitro expansion on genetic stability and tumor formation capacity of stem cells. Stem Cell Rev Rep. 2022;18:241–57. https://doi.org/10.1007/s12015-021-10290-z.
42. Liu T, Zhang L, Joo D, Sun S-C. NF-κB signaling in inflammation. Signal Transduct Target Therapy. 2017. https://doi.org/10.1038/sigtrans.2017.23.
43. Akiyama M, et al. Nuclear factor-κB p65 mediates tumor necrosis factor α-induced nuclear translocation of telomerase reverse transcriptase protein. Cancer Res. 2024;84:939–939. https://doi.org/10.1158/0008-5472.Can-24-0517. Retraction.
44. Mei QR, Liu Z, Zuo H, Yang ZH, Qu J. Idiopathic pulmonary fibrosis: an update on pathogenesis. Front Pharmacol. 2022;12:797292. https://doi.org/10.3389/fphar.2021.797292
45. Théry C, et al. Minimal information for studies of extracellular vesicles 2018 (MISEV2018): a position statement of the international society for extracellular vesicles and update of the MISEV2014 guidelines. J Extracell Vesicles. 2018;7:1535750. https://doi.org/10.1080/20013078.2018.1535750
46. Mansouri N, et al. Mesenchymal stromal cell exosomes prevent and revert experimental pulmonary fibrosis through modulation of monocyte phenotypes. Jci Insight. 2019. https://doi.org/10.1172/jci.insight.128060.
47. Wan X, et al. Mesenchymal stem cell-derived extracellular vesicles suppress the fibroblast proliferation by downregulating FZD6 expression in fibroblasts via micrRNA-29b-3p in idiopathic pulmonary fibrosis. J Cell Physiol. 2020;235:8613–25. https://doi.org/10.1002/jcp.29706.
48. Sun L, et al. Exosomal MiRNA Let-7 from menstrual Blood-Derived endometrial stem cells alleviates pulmonary fibrosis through regulating mitochondrial DNA damage. Oxid Med Cell Longev. 2019;2019: 4506303. https://doi.org/10.1155/2019/4506303.
49. Gao SY, et al. PKM2 promotes pulmonary fibrosis by stabilizing TGF-β1 receptor I and enhancing TGF-β1 signaling. Sci Adv. 2022;8(38):eabo0987. https://doi.org/10.1126/sciadv.abo0987
50. Shi MM, et al. Preclinical efficacy and clinical safety of clinical-grade nebulized allogenic adipose mesenchymal stromal cells-derived extracellular vesicles. J Extracell Vesicles. 2021;10:e12134. https://doi.org/10.1002/jev2.12134.
51. Guiot J, et al. Exosomal MiRNAs in lung diseases: from biologic function to therapeutic targets. J Clin Med. 2019;8(9):1345. https://doi.org/10.3390/jcm8091345

52. Zhang Y, et al. A review of its Classification, isolation Techniques, Storage, diagnostic and targeted therapy applications. Int J Nanomed. 2020;15:6917–34. https://doi.org/10.2147/IJN.S264498. Exosome.
53. Miller MR, Blystone SD. Reliable and inexpensive expression of large, tagged, exogenous proteins in murine bone marrow-derived macrophages using a second generation lentiviral system. J Biol Methods. 2015;2(3):e23. https://doi.org/10.14440/jbm.2015.66
54. Zhao Y, et al. Cortistatin protects against intervertebral disc degeneration through targeting mitochondrial ROS-dependent NLRP3 inflammasome activation. Theranostics. 2020;10:7015–33. https://doi.org/10.7150/thno.45359.
55. Chen S, Zhou Y, Chen Y, Gu J. Fastp: an ultra-fast all-in-one FASTQ preprocessor. Bioinformatics. 2018;34:i884–90. https://doi.org/10.1093/bioinformatics/bty560.
56. Anders S, Pyl PT, Huber W. HTSeq—a python framework to work with high-throughput sequencing data. Bioinformatics. 2015;31:166–9. https://doi.org/10.1093/bioinformatics/btu638.
57. Kim D, Langmead B, Salzberg SL. HISAT: a fast spliced aligner with low memory requirements. Nat Methods. 2015;12:357–60. https://doi.org/10.1038/nmeth.3317.
58. Love MI, Huber W, Anders S. Moderated Estimation of fold change and dispersion for RNA-seq data with DESeq2. Genome Biol. 2014;15(12):550. https://doi.org/10.1186/s13059-014-0550-8
59. Baraniak PR, McDevitt TC. Scaffold-free culture of mesenchymal stem cell spheroids in suspension preserves multilineage potential. Cell Tissue Res. 2012;347:701–11. https://doi.org/10.1007/s00441-011-1215-5.
60. Wang Y, et al. Spheroid formation of hepatocarcinoma cells in microwells: experiments and Monte Carlo simulations. PLoS ONE. 2016;11:e0161915. https://doi.org/10.1371/journal.pone.0161915.
61. Garcia-Romero N, et al. Polyethylene glycol improves current methods for circulating extracellular vesicle-derived DNA isolation. J Transl Med. 2019;17(1):75. https://doi.org/10.1186/s12967-019-1825-3

Publisher's note